Visualization of structural changes and degradation of porphyrin-based battery electrodes

Tom Philipp [a], Gregor Neusser [a], Ebrahim Abouzari-Lotf [b,c], Shirin Shakouri [c], Franziska D. H. Wilke [d], Maximilian Fichtner [b,c], Mario Ruben [c,e,f], Manuel Mundszinger [g], Johannes Biskupek [g], Ute Kaiser [g], Philipp Scheitenberger [h], Mika Lindén [h], Christine Kranz [a,*]

[a] *Institute of Analytical and Bioanalytical Chemistry, Ulm University, Albert-Einstein-Allee 11, 89081, Ulm, Germany*
[b] *Helmholtz Institute Ulm (HIU), Helmholtzstraße 11, 89081, Ulm, Germany*
[c] *Institute of Nanotechnology, Karlsruhe Institute of Technology, P.O. Box 3640, 76021, Karlsruhe, Germany*
[d] *GFZ German Research Centre for Geosciences, Telegrafenberg, 14473, Potsdam, Germany*
[e] *Institute of Quantum Materials and Technology, Karlsruhe Institute of Technology, P.O. Box 3640, 76021, Karlsruhe, Germany*
[f] *Centre Européen de Science Quantique (CESQ), Institute de Science et d'Ingénierie Supramoléculaires (ISIS), Université de Strasbourg, Allée Gaspard Monge, 57000, Strasbourg, France*
[g] *Electron Microscopy of Materials Science, Central Facility for Electron Microscopy, Albert-Einstein-Allee 11, Ulm University, 89081, Ulm, Germany*
[h] *Institute of Inorganic Chemistry II, Ulm University, Albert-Einstein-Allee 11, 89081, Ulm, Germany*

HIGHLIGHTS

- Osmium tetroxide staining and optimized embedding procedure for organic electrode materials.
- Tracing of self-conditioning and degradation of a porphyrin-based cathode material.
- Three-dimensional visualization of organic composite battery electrodes.
- Cathodic electrolyte interphase formation after long cycling times at inner pores.

ARTICLE INFO

Keywords:
FIB/SEM tomography
Wavelength-dispersive X-ray spectroscopy (WDX)
Osmium tetroxide staining
Cu-porphyrin active electrode material
Degradation

ABSTRACT

We present FIB/SEM tomography combined with an optimized embedding procedure and osmium tetroxide staining to trace and visualize the initial self-conditioning step as well as degradation processes of [5,15-*bis* (ethynyl)-10,20-diphenylporphinato]copper(II) (CuDEPP) composite electrodes for the first time. Staining with osmium tetroxide allowed visualizing chemical changes of the active CuDEPP material. Four composite electrode samples prior and after cycling with different cycle numbers in $LiPF_6$ electrolyte (i.e., pristine, one, 200 and 2000 charging cycles) were investigated and for all samples 3D reconstructions with a voxel size of $7.15 \times 7.15 \times 20$ nm^3 were performed. The samples were further analyzed by wavelength-dispersive X-ray (WDX) spectroscopy revealing the insertion of the electrolyte into the active material of the electrode. The formation of an interphase adjacent to the inner pore space of the active CuDEPP material could be unambiguously identified. In addition, Raman spectroscopy results confirmed the self-conditioning and degradation processes of the metalloporphyrin complex.

1. Introduction

The ever-growing need for rechargeable energy storage due to a steadily growing global energy demand faces mankind with challenges in terms of sustainability and ecology [1]. Hence, strong efforts are made towards the development and improvement of earth abundant battery chemistries and electrodes based on renewable organic compounds to replace elements of low abundancy [2]. Electron donor-acceptor metalloporphyrin complexes containing [10,20-diphenylporphinato]copper (II), which were first described due to their optoelectronic properties

* Corresponding author.
E-mail address: christine.kranz@uni-ulm.de (C. Kranz).

[3], are promising candidates for rechargeable electrochemical energy storage devices related to their rich redox chemistry and multielectron transfer as recently shown for a Li-free energy storage device [4]. [5, 15-*bis*(ethynyl)-10,20-diphenylporphinato]copper(II) (CuDEPP) is a highly promising organic redox material with electron donor and acceptor properties for monovalent and divalent post-Li ion batteries [5–8]. CuDEPP has been used as anode material [5,9] and as cathode material [5,10] with high cycling stabilities and excellent rate capabilities. For sodium (Na)-ion cathodes, theoretical capacities up to 187 mAh g^{-1} [8] and for potassium (K)-ion electrodes, capacities of 181 mAh g^{-1} and a capacity retention of 87% over 300 cycles [7] were reported. Recently, CuDEPP has also been used as active electrode material in bivalent magnesium (Mg)-ion batteries [6]. CuDEPP-based electrodes for monovalent ions undergo a self-conditioning step and the electrodes exhibit highly reversible charge and discharge processes [5,7,8,10]. The increased capacity and reduced charge transfer resistance after the initial cycles is attributed to the *in situ* electro-polymerization through the ethynyl moieties. The possible formation of an extended π conjugated network results in improved electronic conductivity [7].

Irrespective of the electrode material, limited lifetimes, leading to capacity loss and power fade of Li-ion and post-Li-ion batteries, are related to complex degradation mechanisms of the battery components, which represents still a major challenge. Microstructural heterogeneity, porosity, and tortuosity of the pores of the electrode material determine the charge transport and with that the performance characteristics [11–13]. In respect to anode and cathode degradation, changes within the electrode material, such as disordering and fracturing of the active material due to volume changes along with changes in composition during charging and discharging lead to undesirable performance losses [14–17]. A multitude of spectroscopic and microscopic techniques are employed to understand electrode degradation processes in LIBs as recently reviewed [18–22]. In respect to the organic CuDEPP composite material, scanning electron microscopic investigations [7,8], X-ray photoelectron [7,8,10], UV–vis [10], Raman [9] and IR spectroscopy [5, 8,10] as well as X-ray diffraction [5,7,8] have been used so far for *in-situ* and post-mortem characterization. Among the microscopic imaging techniques, X-ray tomography as a non-destructive technique has been employed in post-mortem and *in-situ* studies to gain qualitative and quantitative information on structural features, degradation of material and chemical composition of LIBs [23–27] and post-Li battery electrodes (e.g., Na, Mg) [28–30]. Alternatively, FIB/SEM tomography, which may provide improved resolution compared to X-ray tomography [27,31], has been used in post-mortem degradation studies of Zn-air battery electrodes [31] as well as metal oxide based electrodes for LIBs [32–39]. State-of-the-art instruments allow nowadays to achieve resolutions below one nm for SE imaging, whereas the slice thickness of the milling steps is routinely in the range of about 10 nm in FIB/SEM tomography. Automated routines for serial sectioning using a focused Ga^{+}-ion beam for milling and high-resolution secondary electron (SE) or backscattered electron (BSE) imaging generates image stacks that can be reconstructed providing nanoscale information on large sections. Datasets provided by FIB/SEM tomography in the investigation of commercial Li-ion battery cathodes demonstrated a correlation of microstructural features with the performance of the battery and are used as valuable input for simulations [35]. Sample preparation is a crucial aspect in microscopic imaging techniques for battery electrodes. Due to the porous nature of most battery electrode materials, artefacts related to shine-through effects and poor contrast between binder, conductive carbon, and active electrode material are a common issue [40,41] and can be avoided by a suitable sample preparation like embedding [33–35]. Filling the pore space of the electrode sample with e.g., silicone resin minimizes shine-through artefacts and enhances the grayscale contrast between the individual electrode components, which is required for reconstruction methods to set accurately the threshold values [33]. Beam damage of the material is also minimized by embedding the samples. Staining of the embedded material may additionally enhance contrasts for organic components minimizing additionally artefacts in determining the threshold values. Osmium tetroxide (OsO_4) was initially used to stain unsaturated polymers [47] and lipids for the fixation of membranes and reacts with isolated double-bonds to osmate esters [48]. It is the standard staining compound to improve contrast in SE imaging for biological samples [42] and polymers [43]. To date, staining has scarcely been used for energy materials, except for the investigation of Li diffusion and dendrite formation [44,45]. Kato reported OsO_4 as highly suitable compound to selectively stain unsaturated double-bonds [46] by introducing heavy atoms to specific areas of the sample that enhances the contrast due to its increased electron scattering.

In this study, we uniquely take advantage of OsO_4 staining in combination with wavelength dispersive X-ray spectroscopy (WDX) mappings supported by energy dispersive X-ray spectroscopy (EDX). The element distribution, in particular the distribution of Os, within the active material gives for the first-time experimental proof of the electropolymerization and allows us to visualize the electrolyte distribution within the active CuDEPP material. Using WDX mappings with an energy resolution of approx. 5 eV [49] enabled us to distinguish between Os and P, which is a problem in EDX maps due to limited energy resolution of about 120–150 eV [50]. In addition, FIB/SEM tomography of the stained CuDEPP composite electrodes provided information on chemical and structural changes within the CuDEPP material at different cycling states, which gave direct proof of the electro-polymerization of the ethynyl moieties and degradation of the active material after longer cycling. We also observed changes in the internal micro- and nanostructure at different cycling states of the composite electrode materials via 3D reconstruction of the CuDEPP composite material.

2. Experimental procedure

2.1. Electrode preparation and cycling

The synthesis and characterization of the CuDEPP was already described elsewhere in detail [5]. The electrodes were prepared by mixing of 50 wt% of CuDEPP active material, 40 wt% of carbon black (Sigma-Aldrich) and 10 wt% of poly(vinylidene difluoride) (PVDF) binder in N-methylpyrrolidone. The electrodes were made by casting a homogenous slurry on the carbon coated aluminum foil current collector, punched into 11.8 mm discs and further dried at 100 °C overnight. 1 mol L^{-1} lithium hexafluorophosphate ($LiPF_6$) in ethylene carbonate (EC): dimethyl carbonate (DMC): propylene carbonate (PC) (EC: DMC: PC 1 : 3: 1 by volume ratio) was used for Li/$LiPF_6$/CuDEPP cells. A glass fiber filter (GF/D, Whatman) and polypropylene film (PP, Celgard 2400) were used as separator. The mass loading of the electrodes was about 6.0 mg cm^{-2}. The electrochemical experiments for the cells were performed using a 2032 coin-type cell (Hohsen Corp., Japan) with a Biologic VMP3 battery tester. Three cells were charged-discharged for different numbers of cycles under a current density of 200 mA g^{-1} for initial 20 cycles and then 4000 mA g^{-1} for extended cycling using a voltage window of 1.8–4.5 V at 25 °C (Fig. S1a). The first cell was charged once to 4.5 V (Fig. S1b) and the second and third cells were cycled for 200 and 2000 times, respectively, and both then left in a fully charged state. The cycled cells were carefully disassembled inside a glovebox and washed using DMC, and then dried at 80 °C in a vacuum oven overnight. The electrochemical impedance spectroscopy (EIS) measurements were performed using the three-electrode EL-cells (PAT-Cell, EL-CELL) with metallic Li counter and reference electrodes by means of a VMP-3 potentiostat (BioLogic Science Instruments). The spectra were measured between 200 kHz and 50 mHz.

2.2. Sample preparation: Os staining and embedding procedure

Small portions of about 3 mm × 5 mm of the CuDEPP composite electrode material was cut and placed overnight in a sealed container together with a droplet of 4% aqueous OsO_4 solution. Highly volatile

OsO_4 enriches in the gaseous phase and reacts with aliphatic double-bonds present in the sample [47,51]. Os is accumulated at the positions of double bonds of the sample. To avoid artefacts due to beam damage and enhance further contrast for the carbon-based electrode components, the samples were embedded using two-step embedding procedures. In the first step, the sample was immersed into silicone rubber (ELASTOSIL® RT 601 A/B, Wacker Chemie AG, Germany). Silicone rubber was chosen for embedding, as it enhances the contrast between filled pore space and the carbon particles in SEM imaging [35]. Infiltration of the silicone into the porous sample was aided by the application of two vacuum steps (240 mbar, 5 min and 30 min). After the embedding step, the sample was removed from the resin and hardened for 24 h at room temperature. For better handling, the sample was then additionally embedded in epoxy resin (EpoFix, Struers GmbH, Germany) again using the same two-step vacuum embedding procedure with subsequent hardening for 24 h. The resulting epoxy blocks were then grinded and polished using SiC abrasive paper and diamond particle suspensions (monocrystalline 3 µm and 1 µm, Leco Corporation, USA) on Nylon paper (Leco Corporation, USA) to expose the embedded electrode sample. After polishing, the samples were sputtered with an approx. 10 nm thick platinum layer to reduce charging effects during element mapping and FIB/SEM tomography.

2.3. FIB/SEM cross-sectioning and tomography

FIB/SEM cross-sectioning and tomography was performed with a Helios Nanolab 600 (Thermo Fisher Scientific, USA). First, a protective platinum layer with a thickness of approx. 400 nm was deposited at the region of interest using ion beam induced deposition (IBID) with methylcyclopentadienyl trimethyl platinum ($C_9H_{16}Pt$) as precursor. In a subsequent step, a wedge was excavated at 30 kV and 9.3 nA, followed by the excavation of two trenches left and right as well as behind the area of interest. The side walls of the sample block were cleaned by cleaning cross-section routine to ensure a straight and smooth morphology of the side facets. The sample was then turned 90° and tilted 7°. With this geometry a new facet was prepared which intersects one of the side walls in a 45° angle along the complete sample volume. This leads to a well-defined straight line of two artificial intersecting facets, that will be visible in each tomography image at the same location and are helpful for accurate alignment of the image stack during data processing (see Fig. S2). To reduce charging artefacts and to protect the alignment facets, the prepared area was again covered by an approx. 300 nm thick platinum layer deposited by IBID. Finally, the front facet of the block was cleaned via cleaning cross-section at 30 kV and 280 pA.

FIB/SEM tomography was done using the 'slice-and-view' software package (Thermo Fisher Scientific, USA). Automated serial milling steps were recorded at 30 kV and 280 pA with electron image acquisition at 3 kV and 0.64 nA using the through the lens detector (TLD) in BSE mode. The voxel size of the sampled volumes was $7.15 \times 7.15 \times 20$ nm^3.

2.4. Data processing

All obtained electron image stacks were processed using Avizo 9.1.0 Lite (Thermo Fisher Scientific, USA) and the free software package Fiji [52]. First, all images within a stack were manually aligned using the intersection of the side wall and the 45° milled facet as a reference point on all recorded images. Afterwards, a median filter was applied to the whole data set using Avizo Lite followed by a bleach correction using Fiji [53]. Application of the filters enhances brightness and contrast as well as correct differences in brightness among the images of the data stack. Finally, images were binarized, segmented and visualized in 3D using Avizo Lite, the threshold for binarization was determined using Fiji (see Fig. S3).

2.5. WDX analysis

WDX measurements were conducted with a JXA-8530FPlus (JEOL Ltd., Japan) operated at 6 kV, 20 nA, a pixel size of 100 nm and a dwell time of 150 ms per pixel. For detector calibration, a peak search was done on pure metal for copper (Cu) and Os as well as on natural quartz (Si) and apatite (P). For Si and P, the Kα lines were used, while for Cu the Lα and for Os the Mα line was used.

The WDX elemental mappings were processed using Fiji to recolor and extract profiles of the active material. For the profiles, 45 µm long profiles from the raw data were extracted and averaged over a width of ten pixels for noise reduced depiction.

2.6. Transmission electron microscopy (TEM)

Cross-section lamella were prepared using a NVision 40 Ar (Carl Zeiss Microscopy Deutschland GmbH, Germany). First a volume of about $30 \times 10 \times 30$ µm^3 was cut out (compare similar images in Fig. S2) and subsequently transferred to a Cu or molybdenum TEM grid using piezo manipulators and *in situ* carbon deposition. Molybdenum TEM grids were used for HR-TEM as shown in Fig. 2. Then the slab was sequentially thinned at 30 kV using currents from 700 to 80 pA with a final thinning step at 5 kV and 40 pA resulting at a final lamella thickness of about 50 nm. TEM and scanning (S)TEM investigations were carried out using a Talos 200X microscope (Thermo Fisher Scientific, USA) operating at 200 kV. TEM images were obtained using a CETA2 4k CMOS camera. Bright- and dark-field images were recorded with an objective aperture of 20 µm and typical beam tilts of 20 mrad (dark-field mode) were used. Diffraction patterns were obtained using the selected area aperture (camera length 320 mm). TEM EDX mappings were obtained using a Thermo Fisher SuperX detector in STEM mode together with parallel high-angle annular dark-field (HAADF) imaging (Fishione STEM detector). Analyzing of the obtained spectra and images were carried out using the Velox software package.

2.7. Raman spectroscopy

From a small portion of electrode samples embedded in EPON, an approximately 1 µm thick cross-section using a ultramicrotome (EM UC7, Leica Microsystems GmbH, Germany) was prepared and placed on a Si substrate. Raman microscopy images and spectra were recorded using a confocal Raman microscope (alpha 300R, WITec GmbH, Germany) with laser powers smaller than 0.5 mW at an excitation wavelength of 532 nm to avoid damaging the sample while performing averaged image scans with integration times of 1 s. To remove fluorescence effects from the shown Raman spectra the rounded shape background subtraction via the software Project FIVE 5.0.6.46 (WITec GmbH, Germany) was used.

3. Results and discussion

3.1. BSE images (cross-sections)

To obtain morphological and structural information of the internal structure of the composite electrode material, BSE images of FIB-cross-sections of all four embedded electrode samples (pristine, 1 cycle, 200 cycle and 2000 cycles) were recorded at 3 kV. In Fig. 1a), the cross-section of the pristine composite material shows clearly visible well-defined and rod-like CuDEPP particles (dark). These rod-like shapes are in accordance with previous SE images of the active material [7,8]. Furthermore, the embedding of the electrode material in silicone resin clearly enhances the contrast between the filled pore space (light gray), (agglomerates of) the active material, carbon black/binder matrix (dark spots within the light gray pore space) and therefore allows a distinction between the different components (see also non-embedded sample shown in Fig. S4). CuDEPP and the carbon black/binder matrix of the

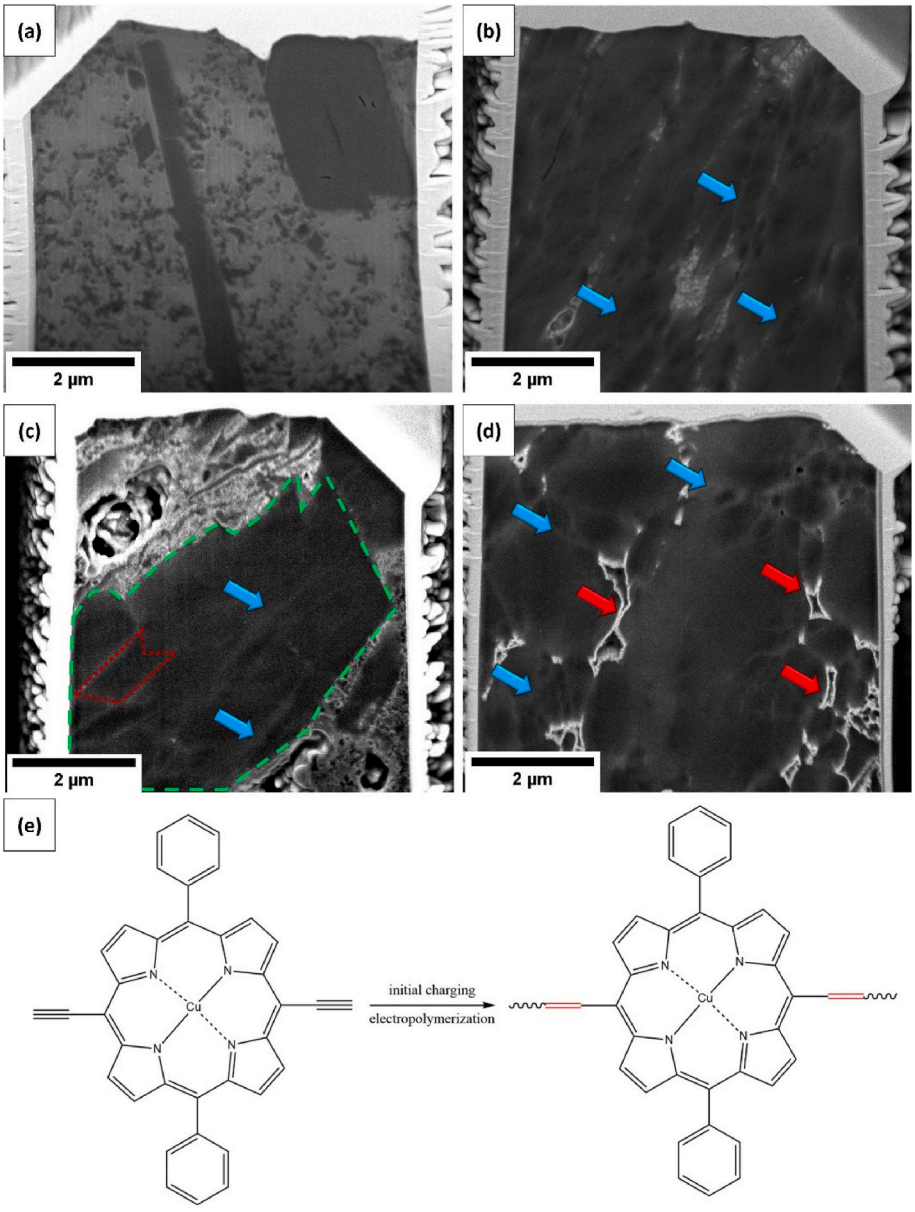

Fig. 1. Backscattered electron images of the front-face of the cross-sections of a pristine CuDEPP composite sample (a) and after one (b), 200 (c) and 2000 cycles (d): samples are embedded in silicone resin and stained with OsO_4. Images were recorded at 3 kV. The silicone resin filled pore space (light gray) as well as osmium-stained areas (bright) within the CuDEPP agglomerates (dark) are visible. The blue arrows indicate grain boundaries within agglomerates of the CuDEPP material. The green framed area in (c) shows an agglomerate of the active material whereas the red framed area represents a single particle within the agglomerate. The red arrows indicate heavily stained areas at the edge of the agglomerates due to degradation processes and interphase formation. Figure (e) shows a scheme of the proposed double-bond formation due to electro-polymerization. (For interpretation of the references to color in this figure legend, the reader is referred to the Web version of this article.)

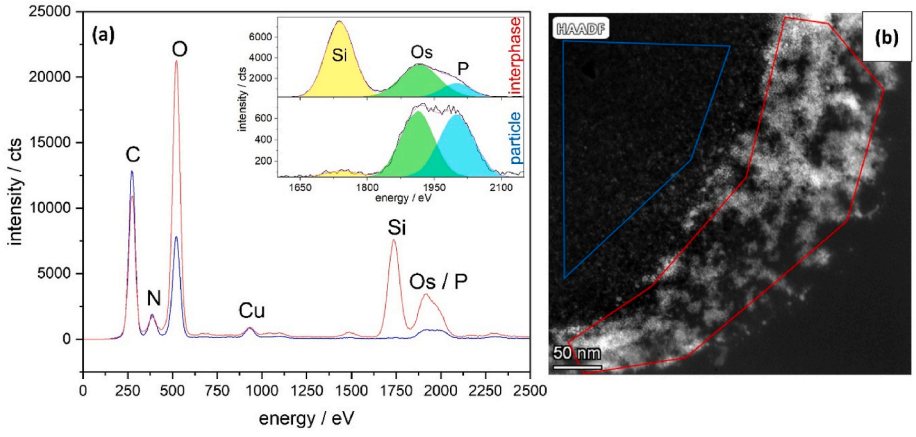

Fig. 2. EDX spectra of the CuDEPP sample after 2000 cycle from the interphase in red and from within a CuDEPP particle in blue (a). The insert in (a) shows the extended spectra of the Si, Os, and P peaks comparing the interphase to the particle as well as deconvolution of the peaks using a Gaussian peak fit to ensure a distinction between Os and P. The EDX spectra were recorded in the areas shown in the TEM image of a cross-section lamella in (b). (For interpretation of the references to color in this figure legend, the reader is referred to the Web version of this article.)

pristine sample cannot be easily distinguished by the gray values of the pixels. The cross-section of the pristine electrode material lacks contrast as pristine CuDEPP is not stained by OsO_4. Aromatic conjugated double-bonds and triple bonds like in pristine CuDEPP particles are not stained [54]. After the initial cycle of the electrode material, staining of the CuDEPP agglomerates is clearly visible. The electrode samples after one, 200 and 2000 cycles reveal all contrast due to OsO_4 staining in the BSE images as shown in Fig. 1b)–d). The brightness gradients within the active material are clearly visible, thus indicating the appearance of non-aromatic double bonds. Furthermore, the staining with Os reveals grain boundaries as areas of increased brightness (blue arrows in Fig. 1b)–d)) within the CuDEPP material that were previously not apparent. It is concluded that the depicted areas of the CuDEPP material in Fig. 1b)–d) are agglomerates (green frame in Fig. 1c)) consisting of several individual particles (red frame in Fig. 1c)). The correlation between increased brightness in BSE images and the content of Os was verified by TEM and TEM EDX measurements exemplary for the sample after 2000 cycles (see Fig. S5). The self-conditioning step of the active material during the initial charge cycle is described as an electro-polymerization step [5,7,8,10] and an increased contrast in the BSE images due to the OsO_4 staining [47] is obtained, therefore it is hypothesized that double-bonds are formed during the initial charging (see Fig. 1e)). In addition to this observed gradient, bright areas at the edges of the agglomerate after 2000 cycles are observed as shown in Fig. 1d) (indicated by red arrows). This significantly increased brightness in the BSE image is related to an enhanced enrichment of Os in this area. This pronouncedly stained layer at the boundary of the CuDEPP material is indicative for a formation of an interphase possibly due to the degradation of the porphyrin moiety leading to an increase in non-conjugated double bonds, which is not known for the decomposition products of the used electrolytes. In Fig. 2a), EDX spectra of the formed interphase (red spectrum) and a CuDEPP particle (blue spectrum) are shown along with the HR-TEM image of the investigated areas (Fig. 2b)). The spectra reveal that both, the particle and the interphase, exhibit a similar Cu content. Therefore, we conclude that CuDEPP material is directly connected to the interphase since the active material is the only present Cu source within the system. However, as depicted in the inset of Fig. 2a), the deconvoluted EDX spectra of Si, Os, and P peaks also show an increase of the P content within the layer. This increase of P intensity within the interphase layer compared to the interior of the CuDEPP particle suggests that the PF_6 ion from the electrolyte might partake in the interphase formation. The same is also visible in the EDX mappings of the interphase, as depicted in Fig. S6. The thickness of this bright layer is around 45 ± 13 nm (N 10) and is in the order (Ångstrom to tens of nanometer range) of described interphase layers formed at battery materials [55,56]. Since this interphase layer is not visible in the BSE images of the cross-sections of the CuDEPP material after one and 200 cycles (Fig. 1b)-c)), the appearance of the bright layer indicates a slow interphase formation during longer cycling of the electrode, and may be associated with the long-term fade in capacity [5] and the increase of resistance [5,10] after the initial self-conditioning process of the electrode material. In agreement, the EIS data reveal significant decline in the charge-transfer resistance (R_{ct}) after initial charging (Fig. S7). This decrease is attributed to the increase in the conductivity because of the *in-situ* electro-polymerization. The charge transfer resistance, R_{ct} decreases slightly over the subsequent cycles before reaching an almost constant value in the range of 1–3 Ω cm^2 after 50 cycles (Fig. S7). In contrast, R_{CEI} appears after initial cycles with very low resistance around 2 Ω cm^2 and continues to increase at a slow rate (Fig. S7c)). This increase agrees well with the BSE images observation of the slow interface formation and the gradual decline in the discharge capacity (Fig. S1a)), as the interface is expected to pose an additional resistance to ion transfer.

3.2. WDX element mapping

WDX mappings were recorded from all four samples, giving information on the element distribution. Since all samples are of heterogeneous nature and contain agglomerates of different sizes, defined sample areas were selected which contain agglomerates of the CuDEPP material in comparable sizes. Several elements were mapped to obtain information on the chemical and structural changes of CuDEPP. Os staining is an indicator of the formation of double bonds from the ethynyl groups through initial charging and changes in the intensities of Os signals are also indicative for chemical changes of the porphyrin structure resulting in non-aromatic double bonds (e.g., after 2000 cycles). Copper (Cu) was mapped as it is contained in the active electrode material. Also, phosphorous (P) was mapped; this provides important information in respect to the diffusion of the PF_6 ion of the electrolyte into the active electrode material and hence reveals structural changes. Usually, EDX and EDX mappings are used to determine the element content and visualize element distributions in energy related materials such as battery electrodes [57,58]. Due to the limited energy resolution of EDX (120–150 eV [50]) in comparison to WDX (about 5 eV [49]), care has to be taken if elements should be mapped which show overlapping signals. For example, overlapping signals are an issue for samples containing Os and P as in our case as well as for Pb/Mo/S [49]. In the case of the Os-stained cycled CuDEPP electrode material, peak overlap occurs between the Os (Mα 1.910 keV) and P (Kα 2.018 keV) originating from the used electrolyte during cycling and Pt (Mα 2.048 keV) used as conductive coating. Hence, it may be difficult to clearly distinguish between the measured element specific peaks using EDX. At the same time WDX may suffer from longer analysis times, as only one element can be measured at a time per WDX spectrometer present at the microscope. In the case of the microscope JXA-8530FPlus used in this study, five spectrometers are available so that five elements can be investigated in one run. The superior energy resolution of WDX as well as the lower limit of detection are advantageous and in the present case ensures a clear differentiation between Os and P. Corresponding WDX mappings for Cu, P and Os of the different electrode samples (pristine, after one, 200 and 2000 cycles) are shown in Fig. 3. The dark areas visible in WDX mappings of the composite electrode in Fig. 3 is related to silicone filled space. Furthermore, a silicon (Si) mapping presented in Fig. S8 visualizes the filled pore space. Areas that exhibit high intensities in the Cu mappings (Fig. 3, red) correspond with CuDEPP particles which occur as agglomerates of sizes in the range of tens of micrometers. As expected, in the mapping of the pristine sample both Os (as described above) and P are absent. The P distribution (represented in cyan color, middle column of Fig. 3) appears to be inhomogeneously distributed throughout the two agglomerates visible in the sample after one cycle and throughout the four agglomerates visible in the 200 times cycled sample. Non-uniform PF_6 ions distribution might be related to different thicknesses of the individual CuDEPP particles within the agglomerates whereby the insertion depth of the PF_6 ion into the active material seems to be related to the particle size and with that by limited diffusion. Interestingly, the distribution of the P intensities in the mapping of the sample after 2000 cycles appears much more homogeneous throughout the visible agglomerate than in the mappings of the one and 200 cycled samples. This can be accounted to an enhanced diffusion of PF_6 into the material and therefore a more thorough penetration of the PF_6 ions due to the longer cycling time. The Os WDX mappings (green color maps shown in Fig. 3) of the samples cycled one and 200 times show an inhomogeneous accumulation within the particles of the CuDEPP agglomerates which coincides with the distribution of P. Profile extractions for Os and P (indicated by the orange lines in Fig. 3) of the one and 200 cycle samples are depicted in Fig. 4a) and b), respectively. Interestingly, the relative intensity pattern of the profiles coincides exceedingly well for both samples. It is therefore plausible that the chemical change of the CuDEPP material by the self-conditioning, which enables the enrichment of OsO_4, is coincident with insertion of the PF_6 into the CuDEPP particles and possibly

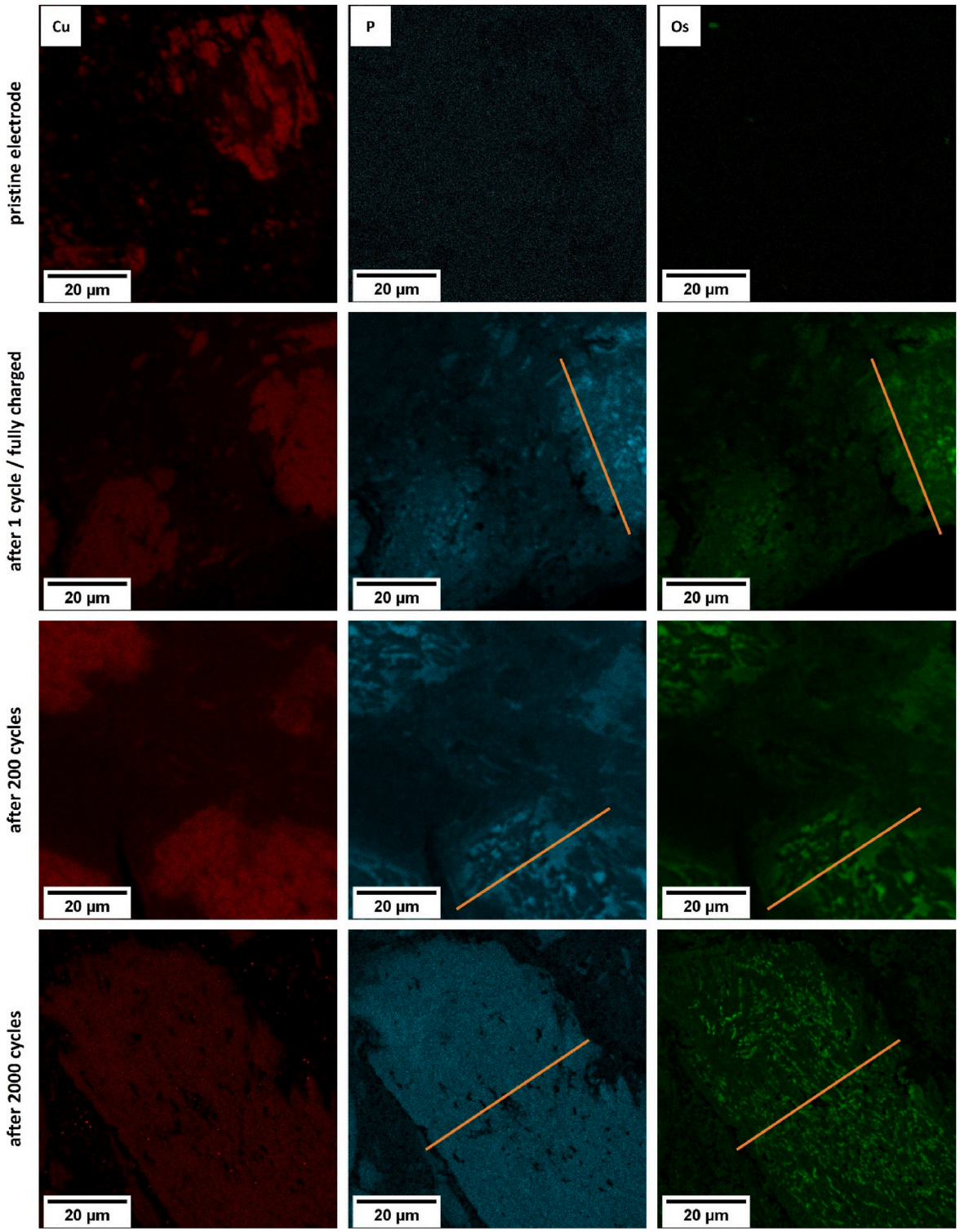

Fig. 3. Element mappings of Cu (red), P (cyan) and Os (green) obtained by WDX. The orange lines in the mappings indicate the positions of extracted intensity profiles for Os and P shown in Fig. 4. It should be noted that the contrast and brightness of the individual mappings shown here are optimized for illustration, and thus no quantitative analysis can be drawn. (For interpretation of the references to color in this figure legend, the reader is referred to the Web version of this article.)

introduces structural changes of the active material. This observation indicates that the structural distortion of the porphyrin ring within the CuDEPP described in literature [7,10] coincides also with a chemical change of the material. To further elucidate this structural change, TEM studies (Fig. S9) were conducted. Therein, the diffraction patterns of the pristine CuDEPP particle and the corresponding dark-field image that exploits the Bragg contrast showing the crystallinity of the pristine CuDEPP material. After the first charging cycle, the diffraction pattern of the CuDEPP particles does not show any distinct diffraction reflexes pointing to an amorphous phase. These findings correspond with X-ray diffractometric investigations of CuDEPP [5,7,8], where e.g., for CuDEPP composite electrode used as Na-ion electrode with PF_6 anions, a gradual loss of crystallinity during initial charging is reported [8]. Our TEM measurements indicate a complete amorphization of the material

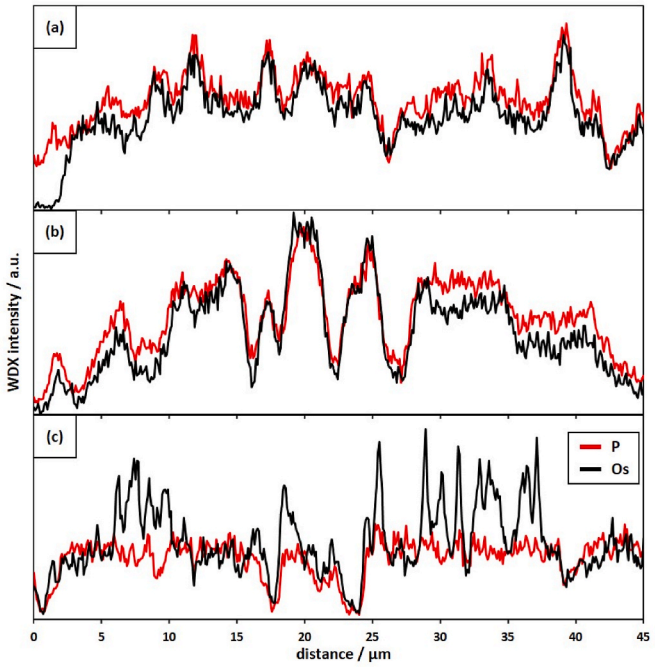

Fig. 4. Relative intensity profile patterns for Os (black) and P (red) extracted from the WDX mappings shown in Fig. 3 (marked with orange lines) for the CuDEPP sample after one cycle (a), after 200 cycles (b) and after 2000 cycles (c). (For interpretation of the references to color in this figure legend, the reader is referred to the Web version of this article.)

already after the initial charging cycle. The observable brightness gradient shown in the BSE images in Fig. 1 is not visible in the Os and P mappings of the cycled material since the spatial resolution of the WDX data (100 nm per pixel) is not sufficient. The CuDEPP electrode that was cycled 2000 times shows Os intensities in the WDX mappings with more distinct elongated stained areas whereas the distribution of P after the 2000 cycles appears to be quite homogeneous compared to the samples cycled only once or 200 times. The extracted intensity profile of the 2000 cycle sample (Fig. 4c)) reveals no distinct coincidence in Os and P distribution. While the P intensity shows a relatively homogeneous course within the agglomerate, the Os intensity shows clear peaks. This strong enrichment of Os at distinct areas reveals a second process that is separate of the self-conditioning and insertion of the PF_6 ion into the active material. These distinct enrichments are visible as elongated stained areas in the WDX mappings of Os and correspond to the bright areas at the edges of the CuDEPP agglomerate shown in the BSE image in Fig. 1d) (red arrows). A possible explanation hereof is that the interphase layer may consist of degraded CuDEPP (decomposed porphyrin) and is composed of material that readily reacts to OsO_4.

3.3. *Three-dimensional visualization of the active electrode material*

To visualize the distribution of the changes within the CuDEPP material in the composite electrode upon cycling, we performed 3D reconstructions of the FIB/SEM tomographic data sets. For a three-dimensional depiction, a segmentation of the material is required. Since changes of the CuDEPP material occur gradually from the borders towards the core of the individual particles (brightness gradient in BSE images shown in Fig. 1), the segmentation of the images is done by thresholding (Fig. S3), whereas the threshold is defined for each data set at the half of the maximum gray value between particle boundary and

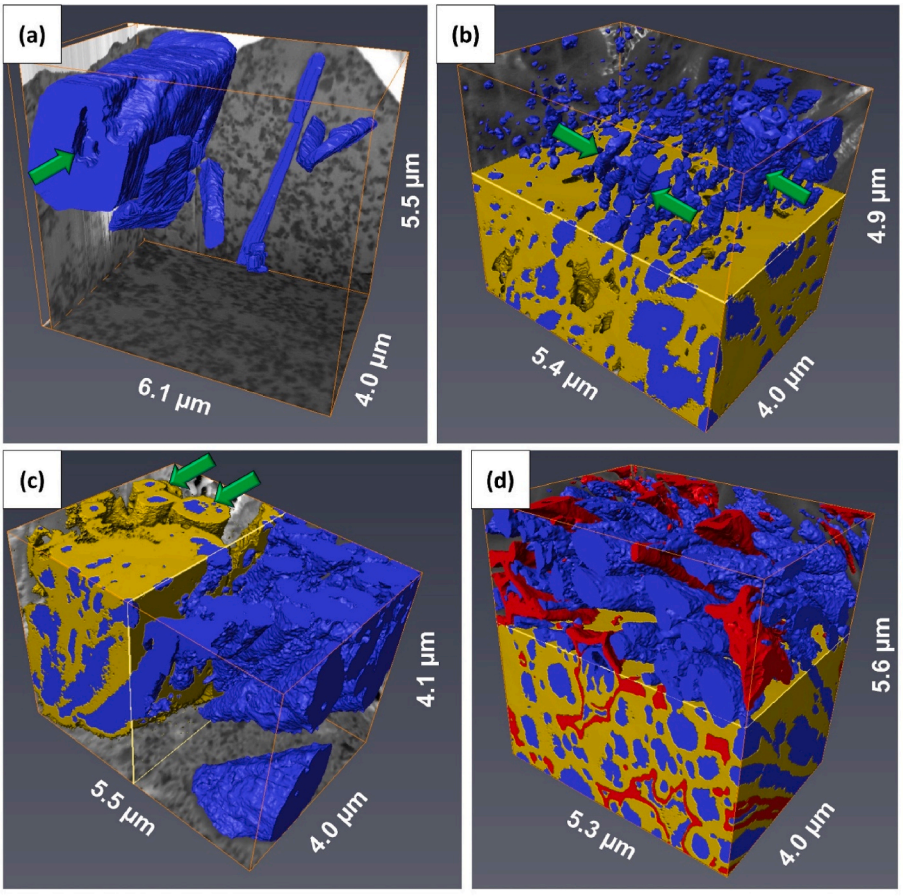

Fig. 5. 3D reconstruction of the pristine CuDEPP electrode (a) and the electrode after one cycle (b), after 200 cycles (c) and after 2000 cycles (d). For better visualization, false color images are presented here: The inner core volumes of the CuDEPP are marked in blue, the clearly stained areas with gray values above the threshold in yellow and the intensively stained volumes after 2000 cycles are marked in red. For an improved and more comprehensible depiction of the cycled samples the yellow volumes are only shown for half of the total reconstructed volume (separated by a clipping plane) to facilitate an insight into the agglomerates of the CuDEPP material. The voxel sizes of the visualizations are 7.15 × 7.15 × 20 nm^3. The green arrows indicate the inner pore space within the agglomerate in (a), elongated core volumes of individual CuDEPP particles in (b) and the entrapment of the inner core region gradient in (c). (For interpretation of the references to color in this figure legend, the reader is referred to the Web version of this article.)

innermost core regions of the particles. Hence, voxels with a lower gray value than the threshold are represented in blue. They correspond to the inner volumes of the particles with low to no Os content present. Voxel with gray values above the threshold are depicted in yellow. The pristine CuDEPP particles (displayed in blue in Fig. 5a)) exhibit a rod-like morphology as already reported [5]. Further, fractures and cavities are present within the pristine agglomerate (green arrow shown in Fig. 5a)). After cycling of the electrode, the samples still show elongated core regions even after 2000 cycles whereas each core region corresponds to a single CuDEPP particle within the agglomerate (Fig. 5b)-d)). These core regions are completely enclosed by the brightness gradient (marked in yellow in Fig. 5). Since the Os and P contents correlates within the particles, it is assumed that a uniform insertion of the electrolyte occurs from all directions into the particles. However, the CuDEPP particles exhibit a gradient and therefore it can be assumed that the complete volume of the active material does not contribute equally to the electrochemical processes during cycling. The strong and distinct enrichments of Os identified in the WDX measurements (Fig. 3d)) for the sample after 2000 cycles extends over parts of the CuDEPP particles (marked in red in Fig. 5d)). Interestingly, this formed layer occurs only locally at the interface towards the inner pore space within an agglomerate and does not enclose single CuDEPP particles. This suggests that direct contact with the electrolyte is a prerequisite for the formation of this layer. The absence of the carbon black/binder matrix in the inner pore space of the agglomerates possibly also contributes to this process since these distinct enrichments of Os are not visible at the outermost parts of the agglomerate (Fig. 3d) and 4c)). Since this strong and distinct Os enrichment is only visible after 2000 charge and discharge cycles, the formation of this layer appears to be a significantly slower process than the self-conditioning process that shows already effect after the initial charging of the electrode material [5]. We assume two different processes to occur, besides the interphase formation after longer cycling times, a fast process occurs directly during the first charging cycle which is apparent by Os staining as well as the loss of crystallinity revealed via the diffraction patterns of the TEM investigations (Fig. S9).

3.4. *Raman spectroscopy*

The CuDEPP agglomerates in the cross-sectional cuts of the electrode samples were also investigated with Raman spectroscopy as shown in Fig. 6. Defined vibrational bands of the pristine CuDEPP electrode

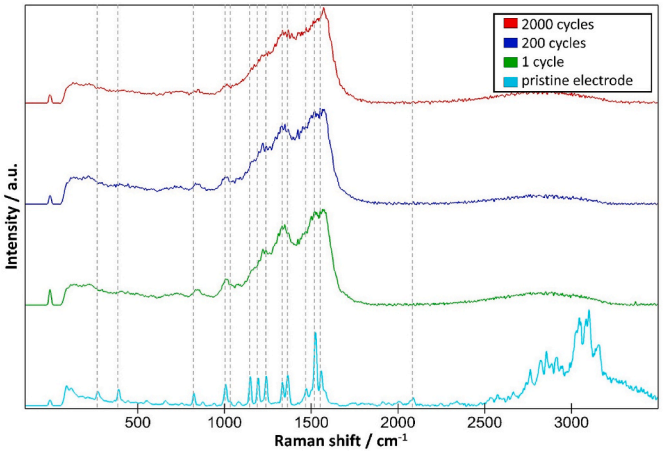

Fig. 6. Raman spectra after background subtraction to remove fluorescence effects of CuDEPP particles of the pristine electrode (cyan), and the electrodes after one cycle (green), after 200 cycles (blue) and after 2000 cycles (red) recorded with an integration time of 1 s. The dotted gray lines indicate the position of the main features visible in the pristine CuDEPP electrode. (For interpretation of the references to color in this figure legend, the reader is referred to the Web version of this article.)

(indicated by the gray dashed lines) are listed in Table S1 and are in accordance with Raman studies reported in the literature [9,59,60]. After the first charging cycle (green spectrum in Fig. 6), the spectrum exhibits already very broad and overlapping bands, which indicate a change in the chemical structure of the material. The broadening of the bands is also visible after 200 and 2000 cycles. In accordance with previous publications, the vibration band of the C≡C bond of the terminal ethynyl groups at 2087 cm^{-1} disappears already after the initial charging cycle and thus confirms a change of the chemical structure in the moiety of ethynyl groups. A putative vibrational band of double-bonds at around 1600 cm^{-1} formed by the *in-situ* electro-polymerization is not directly apparent since it overlaps strongly with the broadened feature of vibrations of the porphyrin structure between 1400 cm^{-1} and 1700 cm^{-1}. However, a general shift of these broad bands towards higher wavenumbers in comparison to the pristine sample is obvious. The broadening of the feature is most likely associated with the insertion of the PF_6 ions into the structure and their strong interaction with the nitrogen atoms of the porphyrin ring [10]. The vibration bands at 1007 cm^{-1} and at 1033 cm^{-1} assigned to in-plane deformation vibrations of the phenyl groups, as well as the band at 824 cm^{-1} corresponding to the wagging of phenyl hydrogens show significant broadening but remain distinct throughout all spectra. The band at 1241 cm^{-1} associated with the stretching vibration between the phenyl groups and the porphyrin structure broadens and overlaps strongly with adjacent bands but remains apparent in the spectra of the cycled samples. Therefore, it can be assumed that the phenyl groups maintain their integrity during the cycling procedure of the electrode material. The vibrational bands at 1334 cm^{-1}, 1365 cm^{-1} and 1472 cm^{-1}, which can be assigned to stretching vibrations of the pyrrole sub-structure as well as the vibrational bands at 1525 cm^{-1} and 1557 cm^{-1}, assigned to the stretching vibration between the methine bridging and pyrrole carbon, merge during cycling into two broad features wherein original bands of the pristine CuDEPP are only vaguely present as shoulders. The matching positions of original bands in the spectrum of the pristine sample with the (shoulders within) broadened and merged features of the spectra in the cycled samples indicate that the general structural features such as the porphyrin ring and the phenyl groups are most likely preserved, however, the peak broadening suggests that to some degree irreversible chemical changes already occur after the first charging cycle accompanied by the insertion of PF_6 into the active material. This is also supported by the merging and decline of the vibrational bands of the C–H bonds in the range from 2500 cm^{-1} to 3500 cm^{-1} as well as the disappearance of the vibrational bands at 269 cm^{-1} and 391 cm^{-1}, respectively. Further, the latter is associated with the stretching vibration of the Cu–N bond and a decrease in this band is either due to the interaction of the nitrogen atoms with PF_6 or an indication of Cu removal from the active material what is so far only known for the CuDEPP material in combination with Mg ions [6]. The interphase layer visible in the BSE images after 2000 cycles (Fig. 1c)) is not discernible in distinct bands of the Raman spectra.

4. Conclusion

Composite battery electrodes containing CuDEPP were investigated in dependence of the cycling number in respect with chemical and structural changes. Element mappings using WDX with high energy resolution show that already during the first charging cycle irreversible self-conditioning or degradation processes occur that are traceable using OsO_4 staining. Raman spectroscopy confirms that this initial process associates with the disappearance of ethynyl moiety. Furthermore, TEM diffraction patterns confirm the amorphization of the CuDEPP particles after initial charging. Therefore, it is apparent that the *in situ* electro-polymerization of the active material occurs during the initial charging process wherein double-bonds are formed as Os is enriched. WDX mappings of CuDEPP agglomerates show the direct correlation of P and Os in the sample after staining and indicates the penetration depth

of the electrolyte into the active material. The brightness gradient, due to Os content visible in BSE images of cross-sections as well as the 3D visualization, reveals that the electrolyte does not completely insert into the active material. This inner part of the active material may not contribute to the performance of the battery. Furthermore, the sample cycled for 2000 cycles shows a distinct and strong enrichment of Os only at the inner pore surface of the particles which does not correlate to P insertion. This clearly reveals a second process after long cycling times of the material. Since this process only occurs locally at the edges to the pore space within the agglomerate of the active material, a lack of contact with the carbon black matrix might have impact on the long-term degradation of the CuDEPP material.

Credit author statement

Tom Philipp: performed data curation - (staining, embedding, FIB/SEM, etc.), evaluated data, and contributed significantly to writing the manuscript.

Gregor Neusser: supervised FIB/SEM tomography, contributed to data evaluation and contributed to writing the manuscript.

Ebrahim Abouzari-Lotf provided the battery material, performed cycling and contributed to writing of the manuscript.

Shirin Shakouri synthesized of active electrode material (CuDEPP).

Franziska D.H. Wilke: performed WDX analysis and contributed to data evaluation.

Maximilian Fichtner supervised battery work and contributed to editing of final manuscript.

Mario Ruben supervised synthesis work and contributed to editing of final manuscript.

Manuel Mundszinger contributed to TEM sample preparation.

Johannes Biskupek performed TEM studies and contributed to editing of final manuscript.

Ute Kaiser supervised TEM studies and contributed to editing of final manuscript.

Philipp Scheitenberger contributed to Raman studies and data evaluation.

Mika Lindén supervised Raman studies and contributed to editing of final manuscript.

Christine Kranz conceptualized the study and supervised the study; edited the final manuscript.

Authorship is limited to those who have contributed substantially to the work reported. All authors have given approval to the final version of the manuscript.

Declaration of competing interest

The authors declare that they have no known competing financial interests or personal relationships that could have appeared to influence the work reported in this paper.

Acknowledgment

The authors acknowledge the Focused Ion Beam Center UUlm for enabling FIB/SEM tomography. The Central Facility for Electron Microscopy (P. Walther) at Ulm University is acknowledged for the staining of the samples with osmium tetroxide and for EPON embedding and cutting of the Raman samples. This work contributes to the research performed at CELEST (Center for Electrochemical Energy Storage Ulm - Karlsruhe) and was funded by the Deutsche Forschungsgemeinschaft (DFG, German Research Foundation) under Germany's Excellence Strategy – EXC 2154 – Project number 390874152 (POLiS Cluster of Excellence).

Appendix A. Supplementary data

References

[1] D. Larcher, J.-M. Tarascon, Towards greener and more sustainable batteries for electrical energy storage, Nat. Chem. 7 (2015) 19–29, https://doi.org/10.1038/nchem.2085.

[2] Y. Lu, J. Chen, Prospects of organic electrode materials for practical lithium batteries, Nat. Rev. Chem. 4 (2020) 127–142, https://doi.org/10.1038/s41570-020-0160-9.

[3] S.M. LeCours, C.M. Phillips, J.C. de Paula, M.J. Therien, Synthesis, transient absorption, and transient resonance Raman spectroscopy of novel electron Donor Acceptor complexes: [5,15-Bis[(4'-nitrophenyl)ethynyl]-10,20-diphenylporphinato]copper(II) and [5-[[4'-(Dimethylamino)phenyl]ethynyl]-15-[(4''-nitrophenyl, J. Am. Chem. Soc. 119 (1997) 12578–12589, https://doi.org/10.1021/ja964436j.

[4] Z. Chen, P. Gao, W. Wang, S. Klyatskaya, Z. Zhao-Karger, D. Wang, C. Kübel, O. Fuhr, M. Fichtner, M. Ruben, A lithium-free energy-storage device based on an alkyne-substituted-porphyrin complex, ChemSusChem 12 (2019) 3737–3741, https://doi.org/10.1002/cssc.201901541.

[5] P. Gao, Z. Chen, Z. Zhao-Karger, J.E. Mueller, C. Jung, S. Klyatskaya, T. Diemant, O. Fuhr, T. Jacob, R.J. Behm, M. Ruben, M. Fichtner, A porphyrin complex as a self-conditioned electrode material for high-performance energy storage, Angew. Chemie Int. Ed. 56 (2017) 10341–10346, https://doi.org/10.1002/anie.201702805.

[6] E. Abouzari-Lotf, R. Azmi, Z. Li, S. Shakouri, Z. Chen, Z. Zhao-Karger, S. Klyatskaya, J. Maibach, M. Ruben, M. Fichtner, A self-conditioned metalloporphyrin as a highly stable cathode for fast rechargeable magnesium batteries, ChemSusChem 14 (2021) 1840–1846, https://doi.org/10.1002/cssc.202100340.

[7] S. Lv, J. Yuan, Z. Chen, P. Gao, H. Shu, X. Yang, E. Liu, S. Tan, M. Ruben, Z. Zhao-Karger, M. Fichtner, Copper porphyrin as a stable cathode for high-performance rechargeable potassium organic batteries, ChemSusChem 13 (2020) 2286–2294, https://doi.org/10.1002/cssc.202000425.

[8] X. Chen, X. Feng, B. Ren, L. Jiang, H. Shu, X. Yang, Z. Chen, X. Sun, E. Liu, P. Gao, High rate and long lifespan sodium-organic batteries using pseudocapacitive porphyrin complexes-based cathode, Nano-Micro Lett. 13 (2021) 71, https://doi.org/10.1007/s40820-021-00593-8.

[9] X.-M. Lin, D.-Y. Wu, P. Gao, Z. Chen, M. Ruben, M. Fichtner, Monitoring the electrochemical energy storage processes of an organic full rechargeable battery via operando Raman spectroscopy: a mechanistic study, Chem. Mater. 31 (2019) 3239–3247, https://doi.org/10.1021/acs.chemmater.9b00077.

[10] X. Feng, X. Chen, B. Ren, X. Wu, X. Huang, R. Ding, X. Sun, S. Tan, E. Liu, P. Gao, Stabilization of organic cathodes by a temperature-induced effect enabling higher energy and excellent cyclability, ACS Appl. Mater. Interfaces 13 (2021) 7178–7187, https://doi.org/10.1021/acsami.0c20525.

[11] S. Lee, A.M. Sastry, J. Park, Study on microstructures of electrodes in lithium-ion batteries using variational multi-scale enrichment, J. Power Sources 315 (2016) 96–110, https://doi.org/10.1016/j.jpowsour.2016.02.086.

[12] Y. Yue, H. Liang, Hierarchical micro-architectures of electrodes for energy storage, J. Power Sources 284 (2015) 435–445, https://doi.org/10.1016/j.jpowsour.2015.03.069.

[13] D.E. Stephenson, B.C. Walker, C.B. Skelton, E.P. Gorzkowski, D.J. Rowenhorst, D. R. Wheeler, Modeling 3D microstructure and ion transport in porous Li-ion battery electrodes, J. Electrochem. Soc. 158 (2011) A781, https://doi.org/10.1149/1.3579996.

[14] D. Chen, D. Kramer, R. Monig, Chemomechanical fatigue of LiMn1.95Al0.05O4 electrodes for lithium-ion batteries, Electrochim. Acta 259 (2018) 939–948, https://doi.org/10.1016/j.electacta.2017.10.179.

[15] H. Liu, M. Wolf, K. Karki, Y.-S. Yu, E.A. Stach, J. Cabana, K.W. Chapman, P. J. Chupas, Intergranular cracking as a major cause of long-term capacity fading of layered cathodes, Nano Lett. 17 (2017) 3452–3457, https://doi.org/10.1021/acs.nanolett.7b00379.

[16] A.O. Kondrakov, A. Schmidt, J. Xu, H. Geßwein, R. Monig, P. Hartmann, H. Sommer, T. Brezesinski, J. Janek, Anisotropic lattice strain and mechanical degradation of high- and low-nickel NCM cathode materials for Li-ion batteries, J. Phys. Chem. C 121 (2017) 3286–3294, https://doi.org/10.1021/acs.jpcc.6b12885.

[17] X. Li, A.M. Colclasure, D.P. Finegan, D. Ren, Y. Shi, X. Feng, L. Cao, Y. Yang, K. Smith, Degradation mechanisms of high capacity 18650 cells containing Si-graphite anode and nickel-rich NMC cathode, Electrochim. Acta 297 (2019) 1109–1120, https://doi.org/10.1016/j.electacta.2018.11.194.

[18] R. Baddour-Hadjean, J.-P. Pereira-Ramos, Raman microspectrometry applied to the study of electrode materials for lithium batteries, Chem. Rev. 110 (2010) 1278–1319, https://doi.org/10.1021/cr800344k.

[19] C.P. Grey, J.M. Tarascon, Sustainability and in situ monitoring in battery development, Nat. Mater. 16 (2017) 45–56, https://doi.org/10.1038/nmat4777.

[20] J.S. Edge, S. O'Kane, R. Prosser, N.D. Kirkaldy, A.N. Patel, A. Hales, A. Ghosh, W. Ai, J. Chen, J. Yang, S. Li, M.-C. Pang, L. Bravo Diaz, A. Tomaszewska, M. W. Marzook, K.N. Radhakrishnan, H. Wang, Y. Patel, B. Wu, G.J. Offer, Lithium ion battery degradation: what you need to know, Phys. Chem. Chem. Phys. 23 (2021) 8200–8221, https://doi.org/10.1039/D1CP00359C.

[21] D. Liu, Z. Shadike, R. Lin, K. Qian, H. Li, K. Li, S. Wang, Q. Yu, M. Liu, S. Ganapathy, X. Qin, Q. Yang, M. Wagemaker, F. Kang, X. Yang, B. Li, Review of recent development of in situ/operando characterization techniques for lithium

battery research, Adv. Mater. 31 (2019) 1806620, https://doi.org/10.1002/adma.201806620.
[22] T. Waldmann, A. Iturrondobeitia, M. Kasper, N. Ghanbari, F. Aguesse, E. Bekaert, L. Daniel, S. Genies, I.J. Gordon, M.W. Loble, E. De Vito, M. Wohlfahrt-Mehrens, Review—post-mortem analysis of aged lithium-ion batteries: disassembly methodology and physico-chemical analysis techniques, J. Electrochem. Soc. 163 (2016) A2149–A2164, https://doi.org/10.1149/2.1211609jes.
[23] O.O. Taiwo, M. Loveridge, S.D. Beattie, D.P. Finegan, R. Bhagat, D.J.L. Brett, P. R. Shearing, Investigation of cycling-induced microstructural degradation in silicon-based electrodes in lithium-ion batteries using X-ray nanotomography, Electrochim. Acta 253 (2017) 85–92, https://doi.org/10.1016/j.electacta.2017.08.161.
[24] Y.-S. Yu, M. Farmand, C. Kim, Y. Liu, C.P. Grey, F.C. Strobridge, T. Tyliszczak, R. Celestre, P. Denes, J. Joseph, H. Krishnan, F.R.N.C. Maia, A.L.D. Kilcoyne, S. Marchesini, T.P.C. Leite, T. Warwick, H. Padmore, J. Cabana, D.A. Shapiro, Three-dimensional localization of nanoscale battery reactions using soft X-ray tomography, Nat. Commun. 9 (2018) 921, https://doi.org/10.1038/s41467-018-03401-x.
[25] Y. Yang, R. Xu, K. Zhang, S. Lee, L. Mu, P. Liu, C.K. Waters, S. Spence, Z. Xu, C. Wei, D.J. Kautz, Q. Yuan, Y. Dong, Y. Yu, X. Xiao, H. Lee, P. Pianetta, P. Cloetens, J. Lee, K. Zhao, F. Lin, Y. Liu, Quantification of heterogeneous degradation in Li-ion batteries, Adv. Energy Mater. 9 (2019) 1900674, https://doi.org/10.1002/aenm.201900674.
[26] X. Lu, A. Bertei, D.P. Finegan, C. Tan, S.R. Daemi, J.S. Weaving, K.B. O'Regan, T.M. M. Heenan, G. Hinds, E. Kendrick, D.J.L. Brett, P.R. Shearing, 3D microstructure design of lithium-ion battery electrodes assisted by X-ray nano-computed tomography and modelling, Nat. Commun. 11 (2020) 2079, https://doi.org/10.1038/s41467-020-15811-x.
[27] R. Moroni, M. Borner, L. Zielke, M. Schroeder, S. Nowak, M. Winter, I. Manke, R. Zengerle, S. Thiele, Multi-Scale correlative tomography of a Li-ion battery composite cathode, Sci. Rep. 6 (2016) 30109, https://doi.org/10.1038/srep30109.
[28] J. Wang, C. Eng, Y.K. Chen-Wiegart, J. Wang, Probing three-dimensional sodiation–desodiation equilibrium in sodium-ion batteries by in situ hard X-ray nanotomography, Nat. Commun. 6 (2015) 7496, https://doi.org/10.1038/ncomms8496.
[29] D. Ledwoch, D.J.L. Brett, P.R. Shearing, E. Kendrick, Investigation of the sodiation and desodiation of hard carbon by electrochemical testing and X-ray computed tomography, ECS Trans. 75 (2017) 81–90, https://doi.org/10.1149/07552.0081ecst.
[30] W. Du, Z. Hao, F. Iacoviello, L. Sheng, S. Guan, Z. Zhang, D.J.L. Brett, F.R. Wang, P. R. Shearing, A multiscale X-ray tomography study of the cycled-induced degradation in magnesium–sulfur batteries, Small Methods 5 (2021) 2001193, https://doi.org/10.1002/smtd.202001193.
[31] M. Biton, F. Tariq, V. Yufit, Z. Chen, N. Brandon, Integrating multi-length scale high resolution 3D imaging and modelling in the characterisation and identification of mechanical failure sites in electrochemical dendrites, Acta Mater. 141 (2017) 39–46, https://doi.org/10.1016/j.actamat.2017.09.008.
[32] J.R. Wilson, J.S. Cronin, S.A. Barnett, S.J. Harris, Measurement of three-dimensional microstructure in a LiCoO2 positive electrode, J. Power Sources 196 (2011) 3443–3447, https://doi.org/10.1016/j.jpowsour.2010.04.066.
[33] M. Ender, J. Joos, T. Carraro, E. Ivers-Tiffée, Three-dimensional reconstruction of a composite cathode for lithium-ion cells, Electrochem. Commun. 13 (2011) 166–168, https://doi.org/10.1016/j.elecom.2010.12.004.
[34] M. Ender, J. Joos, T. Carraro, E. Ivers-Tiffée, Quantitative characterization of LiFePO 4 cathodes reconstructed by FIB/SEM tomography, J. Electrochem. Soc. 159 (2012), https://doi.org/10.1149/2.033207jes. A972–A980.
[35] L. Almar, J. Joos, A. Weber, E. Ivers-Tiffée, Microstructural feature analysis of commercial Li-ion battery cathodes by focused ion beam tomography, J. Power Sources 427 (2019) 1–14, https://doi.org/10.1016/j.jpowsour.2019.04.019.
[36] R. Moroni, S. Thiele, FIB/SEM tomography segmentation by optical flow estimation, Ultramicroscopy 219 (2020) 113090, https://doi.org/10.1016/j.ultramic.2020.113090.
[37] S. Vierrath, L. Zielke, R. Moroni, A. Mondon, D.R. Wheeler, R. Zengerle, S. Thiele, Morphology of nanoporous carbon-binder domains in Li-ion batteries—a FIB-SEM study, Electrochem. Commun. 60 (2015) 176–179, https://doi.org/10.1016/j.elecom.2015.09.010.
[38] T. Shi, Y.-Q. Zhang, Q. Tu, Y. Wang, M.C. Scott, G. Ceder, Characterization of mechanical degradation in an all-solid-state battery cathode, J. Mater. Chem. A. 8 (2020) 17399–17404, https://doi.org/10.1039/D0TA06985J.
[39] Z. Liu, Y.K. Chen-Wiegart, J. Wang, S.A. Barnett, K.T. Faber, Three-phase 3D reconstruction of a LiCoO 2 cathode via FIB-SEM tomography, Microsc. Microanal. 22 (2016) 140–148, https://doi.org/10.1017/S1431927615015640.
[40] M. Klingele, R. Zengerle, S. Thiele, Quantification of artifacts in scanning electron microscopy tomography: improving the reliability of calculated transport parameters in energy applications such as fuel cell and battery electrodes, J. Power Sources 275 (2015) 852–859, https://doi.org/10.1016/j.jpowsour.2014.11.053.
[41] C. Fager, M. Roding, A. Olsson, N. Lorén, C. von Corswant, A. Sarkka, E. Olsson, Optimization of FIB–SEM tomography and reconstruction for soft, porous, and poorly conducting materials, Microsc. Microanal. 26 (2020) 837–845, https://doi.org/10.1017/S1431927620001592.
[42] M. Relucenti, G. Familiari, O. Donfrancesco, M. Taurino, X. Li, R. Chen, M. Artini, R. Papa, L. Selan, Microscopy methods for biofilm imaging: focus on SEM and VP-SEM pros and cons, Biology (Basel) 10 (2021) 51, https://doi.org/10.3390/biology10010051.
[43] R.W. Smith, V. Bryg, Staining polymers for microscopical examination, Rubber Chem. Technol. 79 (2006) 520–540, https://doi.org/10.5254/1.3547949.
[44] M. Zier, F. Scheiba, S. Oswald, J. Thomas, D. Goers, T. Scherer, M. Klose, H. Ehrenberg, J. Eckert, Lithium dendrite and solid electrolyte interphase investigation using OsO4, J. Power Sources 266 (2014) 198–207, https://doi.org/10.1016/j.jpowsour.2014.04.134.
[45] L. Pfaffmann, C. Birkenmaier, M. Müller, W. Bauer, T. Mitsch, J. Feinauer, Y. Kramer, F. Scheiba, A. Hintennach, T. Schleid, V. Schmidt, H. Ehrenberg, Investigation of the electrochemically active surface area and lithium diffusion in graphite anodes by a novel OsO4 staining method, J. Power Sources 307 (2016) 762–771, https://doi.org/10.1016/j.jpowsour.2015.12.085.
[46] K. Kato, Osmium tetroxide fixation of rubber latices, J. Polym. Sci. B Polym. Lett. 4 (1966) 35–38, https://doi.org/10.1002/pol.1966.110040107.
[47] M.A. Parker, D. Vesely, Contrast enhancement and polymer identification in the electron microscope by the formation and staining of unsaturated double bonds, Microsc. Res. Tech. 24 (1993) 333–339, https://doi.org/10.1002/jemt.1070240406.
[48] D.L. White, S.B. Andrews, J.W. Faller, R.J. Barrnett, The chemical nature of osmium tetroxide fixation and staining of membranes by X-ray photoelectron spectroscopy, Biochim. Biophys. Acta Biomembr. 436 (1976) 577–592, https://doi.org/10.1016/0005-2736(76)90442-9.
[49] J.I. Goldstein, D.E. Newbury, P. Echlin, D.C. Joy, C.E. Lyman, E. Lifshin, L. Sawyer, J.R. Michael, Scanning Electron Microscopy and X-Ray Microanalysis, Springer US, Boston, MA, 2003, https://doi.org/10.1007/978-1-4615-0215-9.
[50] J.I. Goldstein, D.E. Newbury, J.R. Michael, N.W.M. Ritchie, J.H.J. Scott, D.C. Joy, Scanning Electron Microscopy and X-Ray Microanalysis, Springer New York, New York, NY, 2018, https://doi.org/10.1007/978-1-4939-6676-9.
[51] G.H. Michler, Electron Microscopy of Polymers, Springer Berlin Heidelberg, Berlin, Heidelberg, 2008, https://doi.org/10.1007/978-3-540-36352-1.
[52] J. Schindelin, I. Arganda-Carreras, E. Frise, V. Kaynig, M. Longair, T. Pietzsch, S. Preibisch, C. Rueden, S. Saalfeld, B. Schmid, J.-Y. Tinevez, D.J. White, V. Hartenstein, K. Eliceiri, P. Tomancak, A. Cardona, Fiji: an open-source platform for biological-image analysis, Nat. Methods 9 (2012) 676–682, https://doi.org/10.1038/nmeth.2019.
[53] K. Miura, Bleach correction ImageJ plugin for compensating the photobleaching of time-lapse sequences, F1000Research 9 (2020) 1–17, https://doi.org/10.12688/f1000research.27171.1.
[54] R. Bruckner, Organic Mechanisms, Springer Berlin Heidelberg, Berlin, Heidelberg, 2010, https://doi.org/10.1007/978-3-642-03651-4.
[55] K. Edstrom, M. Herstedt, D.P. Abraham, A new look at the solid electrolyte interphase on graphite anodes in Li-ion batteries, J. Power Sources 153 (2006) 380–384, https://doi.org/10.1016/j.jpowsour.2005.05.062.
[56] T. Yoshida, M. Takahashi, S. Morikawa, C. Ihara, H. Katsukawa, T. Shiratsuchi, J. Yamaki, Degradation mechanism and life prediction of lithium-ion batteries, J. Electrochem. Soc. 153 (2006) A576, https://doi.org/10.1149/1.2162467.
[57] Y. Wu, N. Liu, Visualizing battery reactions and processes by using in situ and in operando microscopies, Inside Chem. 4 (2018) 438–465, https://doi.org/10.1016/j.chempr.2017.12.022.
[58] T. Sui, B. Song, J. Dluhos, L. Lu, A.M. Korsunsky, Nanoscale chemical mapping of Li-ion battery cathode material by FIB-SEM and TOF-SIMS multi-modal microscopy, Nano Energy 17 (2015) 254–260, https://doi.org/10.1016/j.nanoen.2015.08.013.
[59] M. Atamian, R.J. Donohoe, J.S. Lindsey, D.F. Bocian, Resonance Raman spectra and normal-coordinate analysis of reduced porphyrins. 1. Zinc(II) tetraphenylporphyrin anion, J. Phys. Chem. 93 (1989) 2236–2243, https://doi.org/10.1021/j100343a012.
[60] M. Aydin, DFT and Raman spectroscopy of porphyrin derivatives: tetraphenylporphine (TPP), Vib. Spectrosc. 68 (2013) 141–152, https://doi.org/10.1016/j.vibspec.2013.06.005.